ACCSCIENCE PUBLISHING

Materials Science in Additive Manufacturing

ORIGINAL RESEARCH ARTICLE

Heat transfer model for powder bed temperature management in binder jetting of 316L

Leon Desgagnes[1], Reza Tangestani[1], Waris Nawaz Khan[1], Hongyan Miao[1], Srinivas Pendurti[2], Arunkumar Natarajan[2] and Etienne Martin[1]*

[1]Department of mechanical engineering, Polytechnique Montréal, Montréal, Quebec, Canada

[2]Colibrium Additive, West Chester, Ohio, United States of America

Abstract

Accurate management of powder bed temperature is essential in binder jetting (BJ) to achieve dimensional accuracy and adequate mechanical properties. Three different models using the finite element method operating at different scales were developed in this study to compare their accuracy in predicting the thermal history of the powder bed during the BJ process. The simulated temperatures were compared with *in situ* experimental thermal measurements of the powder bed during printing. The first model relied on 2D Gaussian heat sources to model the movement of infrared lamps, achieving an absolute average error of just 1.5°C with the experimental data, but taking 28 h to simulate only 20 layers using eight CPUs. The second model employed a layer heating (LH) approach to reduce computation time while maintaining accuracy similar to that of the previous model. The second model was able to simulate 200 layers in 33 h with an average error of 1.7°C in comparison with the thermal measurements. The third model combines the LH and lumping approach to further reduce the model computational time, enabling simulation of the full process (2000 layers) in 33 h with an average error of 2.3°C compared to the experimental case. This parametric study suggests that thermal management of the powder bed during BJ can be improved using a combination of infrared lamps above the powder bed and a heated build box. This avoids bleeding, interlayer stitching issues, and other detrimental phenomena regardless of the nesting configuration.

Keywords: Additive manufacturing; Binder jetting; Finite element method; Thermal simulation; Binder drying

***Corresponding author:**
Etienne Martin
(etienne.martin@polymtl.ca)

Citation: Desgagnes L, Tangestani R, Khan WN, *et al*. Heat transfer model for powder bed temperature management in binder jetting of 316L. *Mater Sci Add Manuf*. 2026;5(2):025380088. doi: 10.36922/MSAM025380088

Received: September 19, 2025

Revised: November 4, 2025

Accepted: November 13, 2025

Published online: December 24, 2025

1. Introduction

Additive manufacturing (AM) allows the production of components through sequential deposition of material layers according to the specifications of computer-aided design models. This method enables new possibilities, such as rapid prototyping and fabrication of complex geometries that conventional manufacturing techniques cannot achieve. AM may be used to process a wide range of materials, including Mg,[1] Ni,[2] Al[3-5] alloys, and stainless steel.[6]

Among the emerging technologies in AM, binder jetting (BJ) shows great promise for numerous applications, as it is a solid-state process characterized by relatively low cost and high throughput.[7] Nevertheless, thermal management of the powder remains

a challenge to control the binder viscosity. Efficient production in BJ relies on controlling the powder–binder interaction to ensure sufficient structural integrity and dimensional accuracy of the green part. Infrared lamps and a heated build box are commonly used to control the temperature of the powder bed and the viscosity of the binder. Excessively high powder bed temperatures rapidly increase the binder viscosity, preventing proper penetration into the powder bed. This may lead to an interlayer stitching issue and delamination of the green part.[8] In contrast, if not enough heat is applied, the binder viscosity remains low and propagates undesirably into the powder bed. This phenomenon leads to inaccuracies in the printed geometries referred to as bleeding defects.[9] Part nesting also plays an important role in controlling powder bed temperature. Determining the optimal machine configuration and printing parameters to print consistently defect-free parts is time- and cost-intensive. The finite element method (FEM) allows for establishing a parametric model to predict the impact of parameter input on the thermal history of the powder bed, omitting the need for iterative experimentation.[10,11]

For BJ, FEM has been mostly used to simulate the sintering process.[12-14] However, no existing work has explicitly aimed to predict the complete thermal history of printed components throughout the process. Some studies have focused on understanding the formation of thermally induced defects in laser powder bed fusion (LPBF) applications during printing.[15,16] Given that both LPBF and the BJ drying process described involve the movement of heat sources over a powder bed, many modeling approaches considered for LPBF are, to some extent, relevant in this context. The laser heat source is commonly modeled using a Gaussian distribution for LPBF.[17-19] It consists of a symmetric distribution with the maximum heat flux occurring at the center of the heat source. This approach is known to yield excellent accuracy, with the downside of being computationally costly for large-scale simulations.[20] In the literature, layer heating (LH) is employed to reduce the number of time steps required to simulate the heat input.[20,21] The LH approach avoids the need to simulate heat source movement by applying a uniform heat input to an entire layer. When this method is paired with layer lumping, multiple layers can be processed simultaneously, further improving the computational efficiency.[22,23] To the best of our knowledge, no existing comprehensive model accurately represents the thermal behavior associated with BJ printing.

This work presents the first attempt to simulate the thermal behavior of the powder bed during BJ, with the aim of enhancing powder bed thermal management and reducing part defects. Three models were proposed based on the different approaches to simulate the heating source. The first model (Model 1), called the incremental heating model, uses a 2D Gaussian moving heat input, replicating the movement of the lamps. The second model (Model 2) is referred to as the single LH model because the LH method is applied to an entire layer at a time. The third model (Model 3), named the multiple LH model, uses the combination of the LH method and the lumping method to simulate multiple layers at a time. All three model results were compared with the *in situ* thermal measurement for each build layer. The impact of each heating method on the accuracy and simulation time was discussed.

2. Materials and methods

2.1. Feedstock material

The powder material used in this study was gas-atomized 316L stainless steel powder provided by Sandvik (Sweden). The particle size distribution was measured with the CAMSIZER X2 system (Microtrac MRB, Germany), obtaining D10, D50, and D90 values of 9 μm, 20 μm, and 40 μm, respectively. The powder particles were primarily spherical, with a small proportion of satellite particles adhering to larger particles, as shown in Figure 1. The nominal composition of the 316L stainless steel powder is provided in Table 1.

2.2. BJ process

The specimens were printed on the H2 metal BJ machine (Colibrium Additive, United States [US]) using Colibrium Additive's proprietary water-based binder to generate data for validating thermal models. In total, 27 specimens of two different formats were printed, with the dimensions (length × width × height) being 19 × 19 × 18 mm and 90 × 15 × 15 mm for Format 1 and Format 2, respectively. Specifically, five specimens of Format 1 and 22 specimens of Format 2 in two different orientations were disposed

Table 1. Nominal chemical composition of 316L stainless steel powder

Element	Composition (wt. %)
Fe	Balance
Cr	16.50–18.00
Ni	10.00–13.00
Mo	2.00–2.50
Mn	2.00
Si	1.00
N	0.13
O	0.06
P	0.04
C	0.03

of on the print bed, as shown in Figure 2A. The distance between the specimens varied between 9 mm and 50 mm. All the specimens were built starting 1 mm above the build plate, and the final build height was 19 mm. The printing parameters used to produce the specimens are presented in Figure 2B.

The GE H2 BJ machine was equipped with a heated powder bed to facilitate thermal management of the powder bed and control the binder viscosity. Heating elements were positioned close to the base plate and four build box walls. For this work, the build box components were maintained at a constant temperature of 65°C. The top surface of the powder bed was exposed to the air of the chamber. Figure 3 provides a detailed representation of the BJ printing process, representing both the recoating (Figure 3A) and the binder deposition step (Figure 3B). The recoater speed was kept constant at 90 mm/s during the application of a new layer. Two heating lamps were positioned ahead and behind the recoater, respectively, to help control the binder temperature and viscosity. The heat generated by the lamp positioned ahead of the roller heated the previously deposited layer containing powder and binder–powder mixture, as shown in Figure 3A. The trailing lamp heated the newly deposited powder layer in preparation for the upcoming binder deposition. Each lamp covered the entire width of the powder bed (y-axis) as it moved along its length (x-axis). Power produced by each lamp (20 W) was kept constant during the entire printing process. After the recoater moved back to its initial position, the printhead moved from the opposite side of the powder bed and selectively applied binder to the newly deposited layer, as shown in Figure 3B. The binder set time (Figure 2B) corresponded to the time between the movement of the printhead in layer n and the recoater in layer n+1.

2.3. Finite element modeling of the BJ process

An Ansys Parametric Design Language (APDL)-based finite element model was used to simulate the thermal

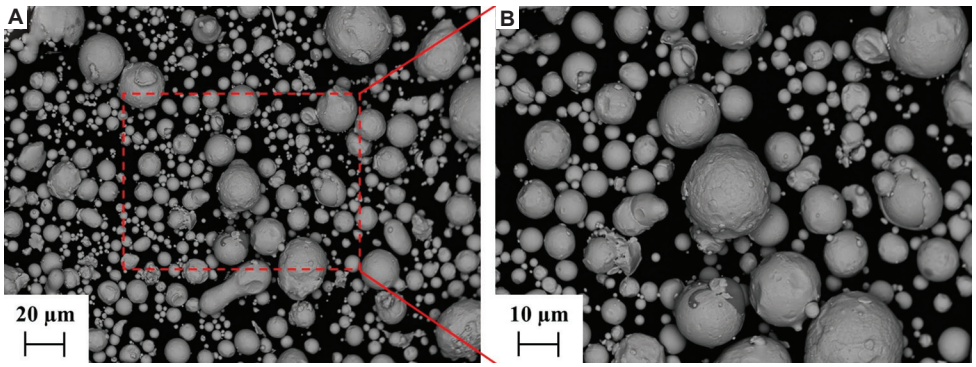

Figure 1. Scanning electron microscopy images showing the morphology of 316L stainless steel powder under different scales: (A) 20 µm and (B) 10 µm. Magnifications: (A) × 500, (B) × 1000

A

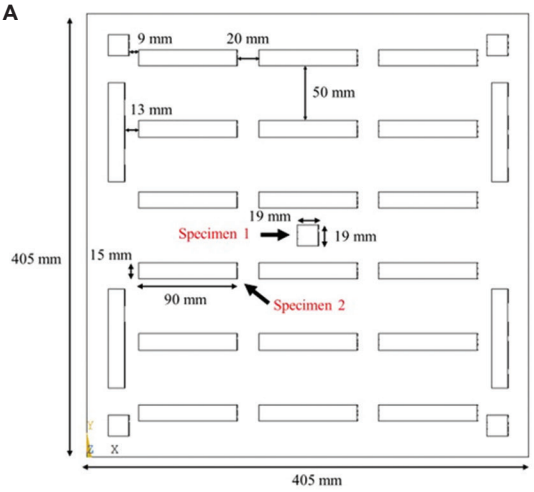

B

Build parameter	Value
Build box wall temperature (°C)	65
Base plate temperature (°C)	65
Lamp power, P (W)	20
Recoating speed, v (mm/s)	90
Powder layer thickness, t (µm)	100
Binder set time (s)	15
Binder saturation (%)	100

Figure 2. Summary of the printed specimens. (A) Schematic of the different printed specimens (Formats 1 and 2) in the powder bed. (B) Build parameters

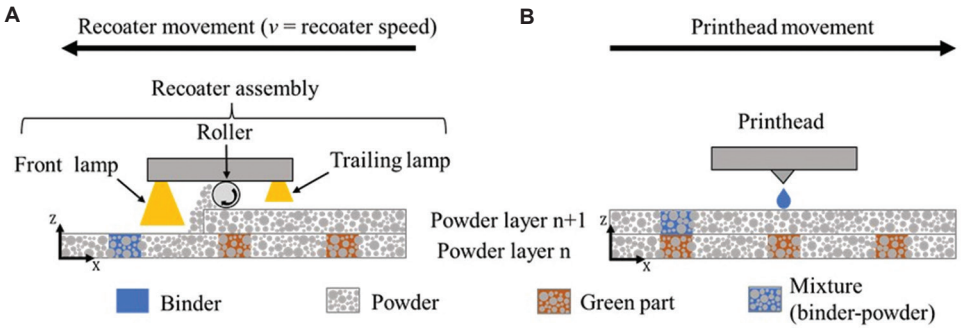

Figure 3. Schematics (not to scale) of (A) the recoater assembly composed of a front lamp, trailing lamp, and roller; and (B) the printhead with the different materials involved in the process identified

history of the BJ process. The nodal temperature of the model was calculated following Equation (1) from Fourier's 3D heat conduction law:

$$\frac{\partial}{\partial x}\left(k\frac{\partial T}{\partial x}\right)+\frac{\partial}{\partial y}\left(k\frac{\partial T}{\partial y}\right)+\frac{\partial}{\partial z}\left(k\frac{\partial T}{\partial z}\right)+q'''=\rho C_p\frac{\partial T}{\partial t} \quad (1)$$

where k is the thermal conductivity (W/m/K), T is the temperature (K), q''' is the volumetric heat flux generated by the lamps (W/m^3), ρ is the density (kg/m^3), C_p is the specific heat capacity (J/kg/K), and t is the time (s). Setting initial and boundary conditions was necessary before attempting to solve the second-order differential equation. The initial state of the system, represented in Equation (2), formed the initial condition:

$$T(x,y,z,0)=T_0 \quad (2)$$

where T_0 is the initial temperature (K) of the powder bed. Since the simulation domain in this study was limited to the powder bed, the various exposed surfaces were subjected to a combination of heat transfer mechanisms, including conduction, convection, and radiation. All heat transfer mechanisms involved in the model's boundary conditions are defined in Equation (3):

$$-k\frac{\partial T}{\partial n}+h(T-T_\infty)+\sigma\varepsilon\left(T^4-T_\infty^4\right)=0 \quad (3)$$

where n is the direction normal to the surface, h is the convective heat transfer coefficient (W/m^2/K), T_∞ is the temperature of the chamber (K), ε is the surface emissivity coefficient, and σ is the Stefan–Boltzmann constant (W/m^2/K^4). Radiation was neglected, as the temperature difference between the powder bed and the air of the chamber during most of the process was under 20 K. Notably, the temperature spikes generated by the movement of the infrared lamp lasted less than four seconds and were localized over a small area of the powder bed.

Consequently, Equation (3) can be rewritten as follows:

$$-k\frac{\partial T}{\partial n}+h(T-T_\infty)=0 \quad (4)$$

The simulation process was fully automated, from file creation to managing simulation results using a shell script, increasing the overall efficiency of the model. This approach proves particularly useful in the context of parametric studies, as many different simulation cases can be created and run simultaneously. Figure 4 shows the specific structure and framework of this automation method. Specific sets of printing parameters, such as those presented in Figure 2B, were used as inputs in a Python script to generate APDL input files. The input files contained the material properties, the geometry of the printed specimens, the mesh, the initial and boundary conditions, as well as the commands to model the different steps of the BJ process. Ansys batch mode was used to execute the simulations, providing the ability to run several simulations simultaneously or sequentially from a single command. Once the model was solved, the nodal temperatures that matched the location of interest from the experimental data were used for validation with the thermal camera data.

2.4. Heat source models

Modeling the movement of heat sources from the front and trailing lamps requires multiple time steps and becomes a computational burden when simulating a high number of layers. Optimizing the time discretization is an efficient approach to improve the model's computational efficiency. Three different methods were used to simulate the heat sources from the two lamps attached to the recoater. Model 1 is referred to as the incremental heating model, Model 2 as the single LH model, and Model 3 as the multiple LH model. Concepts from LH and layer lumping were integrated into the multiscale modeling approach of this study to improve computational efficiency without

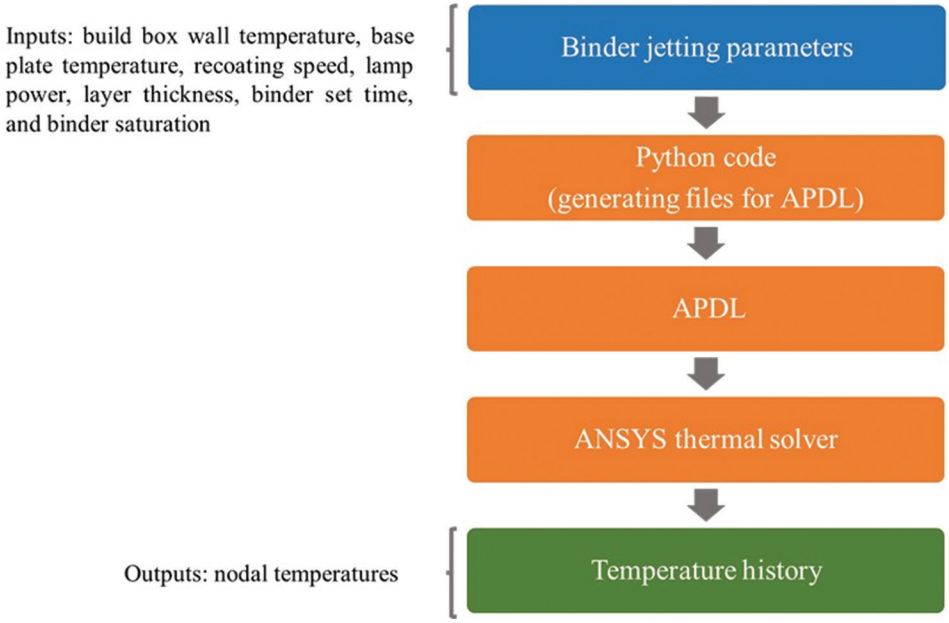

Figure 4. Flowchart of the computational framework
Abbreviation: APDL: Ansys Parametric Design Language

sacrificing accuracy significantly.[22,23] The heat input from the lamps was modeled as a volumetric heat input, while the boundary condition resulting from the convection between the air of the chamber and the top of the powder bed was modeled as a heat flux for the three models. This allows for compensating for the inability of the Ansys software to apply more than one heat flux to a surface at a time.

2.4.1. Incremental heating model (Model 1)

For Model 1, the movement of the heat sources on the recoater was modeled with several time steps. A sensitivity study was conducted to determine the optimal number of time steps (40 increments). Inspired by the 2D Gaussian moving heat input suggested by Goldak *et al.*[18] for the weld heat source, the volumetric heat flux was computed for every element at each time step using Equation (5):

$$q''' = \frac{\eta P}{H\pi R^2} e^{(-(\frac{x-x_0}{B})^2)} \quad (5)$$

where q''' is the volumetric heat flux (W/m^3), H is the top layer thickness (100 µm; Figure 2B), R is the radius of the sensor (0.0127 m), and η is the absorptivity of the material (0.45). To simplify the experimental requirements of this study, it was assumed that the absorptivity of the CO_2 laser in iron powder[24] was sufficiently similar to the conditions of this study. This assumption was based on the fact that the heat sources shared a similar wavelength (10 µm) with the CO_2 laser and that 316L powder is an Fe-based alloy. P (W) represents the maximum power of the lamps (20 W; Figure 2B). As shown in Figure 5A, the distance between each element and the center of the heat sources can be computed using x as the element center position (m) and x_0 as the heat input center position (m). The positions of the heat sources evolve over time and are dependent on the recoater speed. B is the heat concentration parameter (0.0266 m) calibrated experimentally, which is proportional to the diameter of the heat sources and allows adjustment between the width of the heat sources and lamps.

A PM160T-HP thermal sensor power meter (Thorlabs, US) was positioned in the center of the powder bed to ensure the matching of the sensor's top surface with the powder bed. The recoater was then moved along the powder bed with the lamps active, but without the roller action involved to prevent the sensor from being buried by powder. Power data at regular intervals of 0.1 s were acquired, and the recoater moved over the bed at constant speeds of 50, 60, and 90 mm/s. This method took advantage of the sensor area to measure power and identify the maximum heat flux, eliminating the need to consider the fraction of heat absorbed within its radius, as done for the LPBF process.[15] Based on this approach, Equation (5) consisted of the sensor's radius instead of the heat source's radius. Finally, the heat flux was made volumetric by assuming that the heat absorbed by the sensor only penetrates through the top layer.

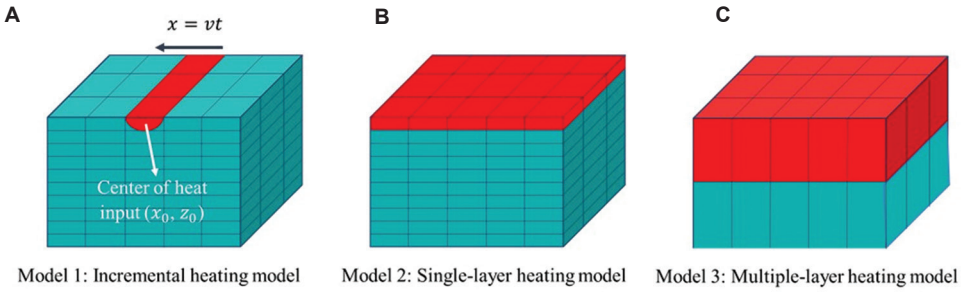

Figure 5. Schematics of the heat input approaches. (A) The incremental heating model (Model 1), where x is the position of the center of the beam, v is the build speed, and t is the time. (B) The single-layer heating model (Model 2). (C) The multiple-layer heating model (Model 3) integrates layer heating and layer lumping

2.4.2. Single-LH model

To imitate the addition of a layer in a single time step, we simultaneously activated and heated the entire layer, as shown in Figure 5B. Equation (6) represents the quantified volumetric heat input for this LH method:

$$q''' = \frac{N \times E \times \eta}{H \times A_{sensor} \times t_{layer}} \quad (6)$$

where E is the total energy (J) captured by the thermal power sensor throughout the complete motion of the lamps over the print bed, computed by integrating the power data over time; A_{sensor} is the area of the sensor (0.000510 m^2) used in the experiment; t_{layer} is the real time (s) needed for the lamps to travel over the powder bed; and N is the calibration coefficient (0.525) that allows the LH method to reproduce volumetric heat input from the incremental approach over one layer. LH is mostly used with a calibration coefficient of 1 for thermo-mechanical simulation in LPBF.[20,21] It was set to 0.525 in our study to ensure the convergence of results from Models 1 and 2. This can be explained by the fact that heat loss through conduction in LPBF is more pronounced due to the higher thermal conductivity of the molten and solidified metal compared to the powder in BJ.[25] Moreover, Imani Shahabad *et al.*[26] showed that radiative losses, which were neglected in this study, account for approximately 20% of the total thermal energy loss in LPBF applications. Therefore, the laser heat input must be scaled down using a calibration coefficient between 0 and 1 to account for the significantly lower heat loss in BJ.

2.4.3. Multiple-LH model

It is also possible to group and simulate numerous layers concurrently to reduce computational time, as shown in Figure 5C. This approach, known as layer lumping, combined with LH, allows for applying the heat input simultaneously to a group of layers. Bayat *et al.*[22] and An *et al.*[23] demonstrated that lumping up to 20 layers can produce accurate results in the LPBF process. To further improve the efficiency of Model 3, the LH method was applied to the equivalent of 10 layers at a time. The group of layers was meshed as a single, thicker layer, significantly reducing the number of elements in the model and enhancing the advantages of the lumping method. Equation (6) was used without changing any parameter; however, to accurately replicate the process, the duration of each step in the calculations was multiplied by the number of lumped layers, ensuring that the different heat exchange mechanisms operate for the same length of time as they would in a traditional layer-by-layer approach.[22]

2.5. Powder bed geometry and meshing

Figure 6 presents the finite element model of the powder bed, with a length and width of 405 mm each, and a print height of 18 mm, used for drying simulations.

The simulation employed linear elements with a height matching the thickness of deposited powder layers. For Model 1, the meshing was programmed to ensure that the elements were aligned in the x and y directions (Figure 7A) using the VMESH command. The mesh size was not uniform to adequately integrate the printed geometry area, as element boundaries must coincide with the specimen boundary during the simulation. Alignment among the elements of the print bed required additional manipulation, but is essential to effectively simulate the behavior of the recoater, including the deposition of powder and the incremental heating discussed in Section 2.3. Since the LH methods did not require aligned elements, the VMESH was used to generate the mesh without additional manipulations, as shown in Figure 7B. A mesh independence study was conducted to assess the impact of element size. The mesh of the incremental and LH models showed no change in results for most of their surface when refining the mesh from 5 mm to 2.5 mm. Another limiting factor was the nesting of the specimens; the smallest distance between specimens (9 mm; Figure 2A)

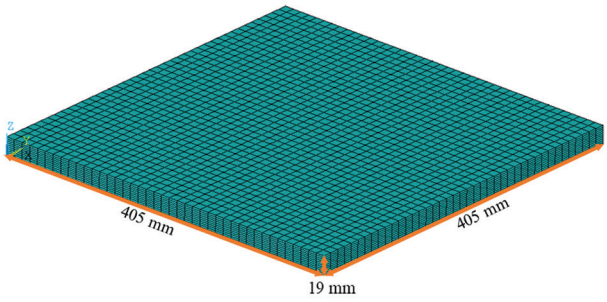

Figure 6. Schematic of the finite element model of the binder jetting powder bed used to simulate the drying process

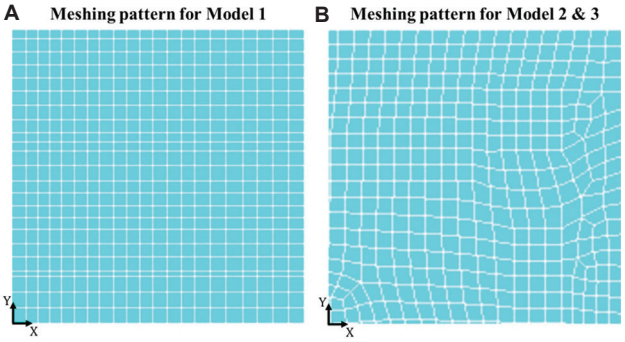

Figure 7. Meshing patterns created using VMESH for (A) Model 1 and (B) Models 2 and 3 using the same element size for the ESIZE command

required a mesh size of 5 mm to adequately capture the temperature gradient between the powder and printed specimens. Figure 8A illustrates the artificial cooling of the loose powder between specimens using a 10 mm element size in the model. In contrast, Figure 8B demonstrates the correction of this issue by refining the mesh size to 5 mm.

2.6. Boundary conditions from experimental calibration

Figure 9 shows a comparison between the chamber's thermal profiles experimentally measured during printing using thermocouples and the temperature distribution in the simulations. The temperature inside the chamber increased due to convective heat transfer between the heated powder bed and air. Results demonstrated that the air in the chamber, initially at 25°C, increased logarithmically to 42°C. The model used a linear increase method to reduce the computational time. Since the deposition of each new layer changes the interface between the elements and air, an algorithm was used to adjust the interface's location, thereby removing the surface convection from the newly buried elements and reapplying it to the uppermost active elements.

To reduce calculation time, the aluminum build box was not incorporated into the model. However, this means that heat transfer by conduction between the powder bed,

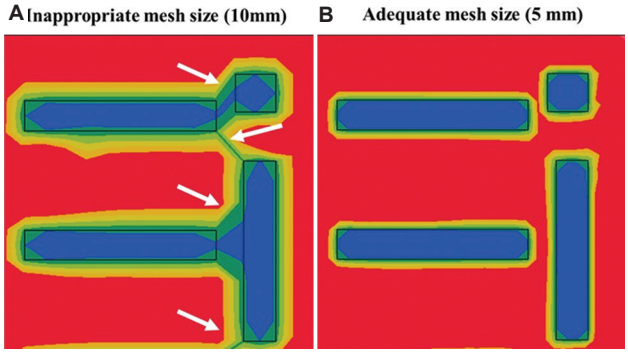

Figure 8. Meshing patterns created using VMESH and the same element size for the ESIZE command for (A) Model 1 and (B) Models 2 and 3. The white arrows indicate thermal artefacts resulting from an insufficient number of elements to accurately capture the thermal gradient

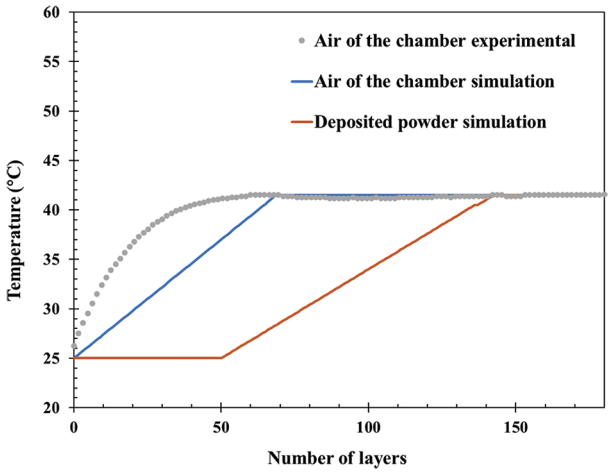

Figure 9. Comparison between the temperature distribution of the air in the chamber and the distribution used for the simulations

the base plate, and the walls of the build box cannot be computed. To address this issue, the heat transfer between the base plate and the walls of the build box, which were kept at a constant temperature of 65°C, was modeled using convection. The convection coefficient of each surface was calibrated in the model using a special experimental procedure. Seventeen thermocouples of type-K were positioned in the powder bed filled with 316L powder, as shown in Figure 10A. The base plate and the four powder bed walls were heated to 130°C for 24 h, while the air of the BJ chamber was simultaneously and gradually heated from 25°C to 60°C. The heating profiles for the build box and the chamber air are presented in Figure 10B and C, respectively. The powder was only heated by the build box, and the infrared lamps attached to the recoater were not used.

The thermocouple experiment was then reproduced in the simulation software with an array of different combinations of convection coefficients for the base plate

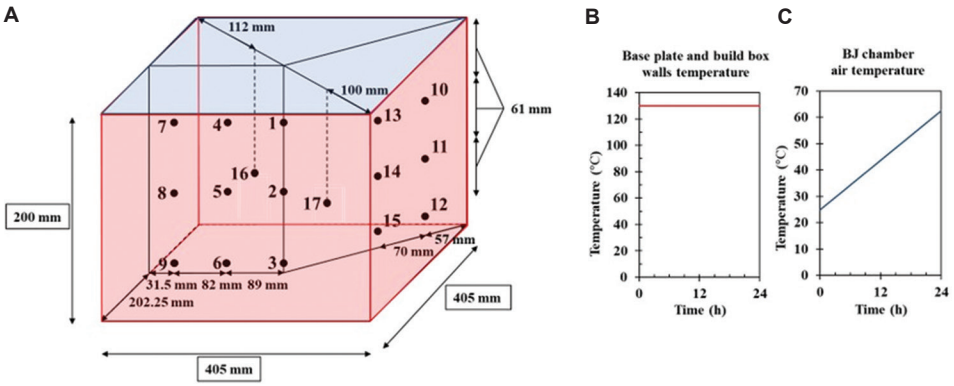

Figure 10. Summary of the calibration process for the boundary conditions. (A) Schematic representation of the thermocouple positioning within the powder bed during the experimental procedure to establish the boundary conditions, with boundary conditions differentiated by distinct colors: red indicating the base plate and the build box walls, whereas blue indicates the binder jetting (BJ) chamber air. Heating profiles for the (B) base plate and the build box walls, and (C) BJ chamber air

(h_{bottom}), build box walls (h_{walls}), and upper surface of the powder bed (h_{top}). Figure 11 shows a schematic of the applied boundary conditions. Convection coefficients of 15, 20, and 30 W/m^2/K for h_{bottom} and h_{walls}, as well as 7.5, 15, and 30 W/m^2/K for h_{top}, were used across a total of 27 cases. The average error for each thermocouple was computed for each simulated case, and the optimal parameters with the lowest maximum error and the lowest average error for all thermocouples were used. In Figure 12, the thermal profiles acquired from the thermocouples were compared with the results from the simulation using optimum coefficients (h_{bottom} = 15 W/m^2/K, h_{walls} = 20 W/m^2/K, and h_{top} = 7.5 W/m^2/K). The maximum (13.2°C) and minimum (1.4°C) average errors were observed at thermocouples 10 and 3, respectively.

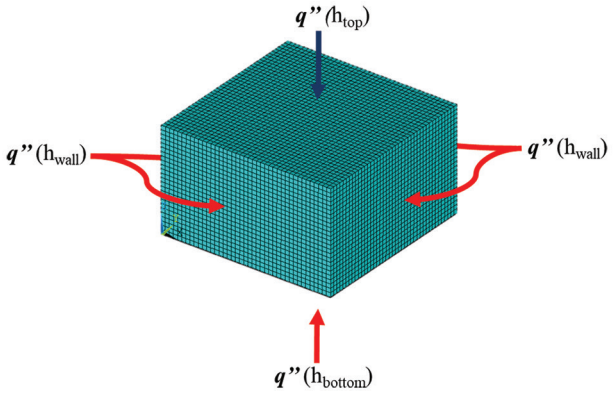

Figure 11. Schematic of the boundary conditions involved in modeling heat transfer from the powder bed

2.7. Powder deposition

The "element birth and death" technique was used to simulate the gradual deposition of powder onto the bed and to reduce the computational time. Initially, the model representing the print bed at the end of the process was created. Then, the Ansys command EKILL was used, and all the elements unrelated to the initial stage of the process were deactivated. Although the deactivated elements remained in the model, their material properties were significantly reduced, preventing them from contributing to the heat transfer process.[27] Once the calculation started, elements were gradually reactivated according to the machine deposition pattern as new layers were added, using the EALIVE command. Figure 13 illustrates how the element birth and death technique affects the elements composing the powder bed. Upon activation, the nodal constraints on the top surface of the elements were removed using the DDELE command, allowing the elements to interact freely with the powder bed.

To account for the differences in volume and specific heat capacity between the air and the powder in the supply bed, it was determined that after 50 layers, the deposition temperature of the powder started increasing linearly until it stabilized at the air temperature (Figure 9).

2.8. Temperature-dependent material properties

Isotropic temperature-dependent properties, such as thermal conductivity, specific heat capacity, and density values for temperatures ranging from 25°C to 125°C, were assigned to powder compacted in the powder bed, the binder-powder mixture, and the green (binder–powder mixture dried) parts. For 316L, the powder density (4,830 kg/m^3) was obtained by measuring the mass, size, and volume of the powder bed. Knowing the relative density of the powder material, the specific heat capacity (509 J/kg/K at 25°C) and thermal conductivity (0.14 W/m/K at 25°C) were obtained from literature.[28] For the water-based binder, the water properties from the

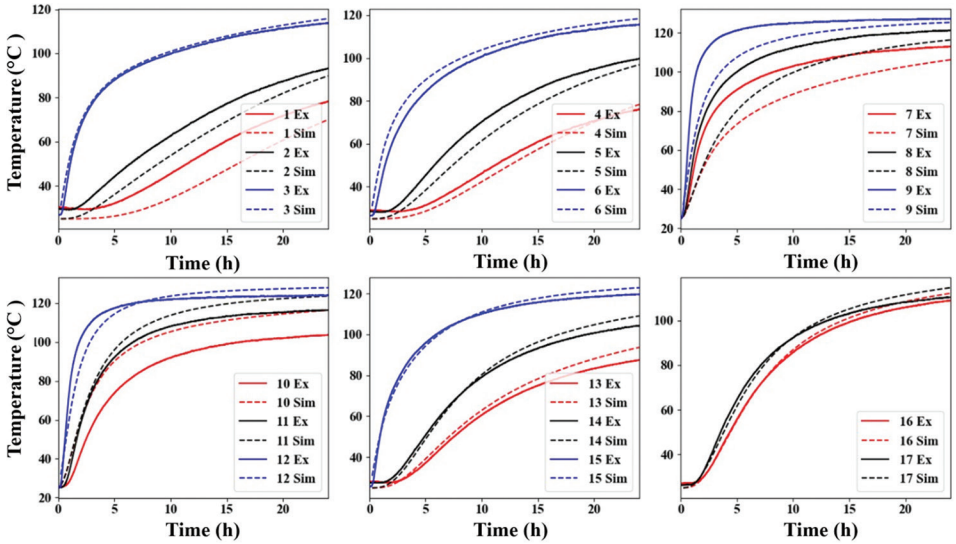

Figure 12. Comparison between the simulation results and the experimental thermocouple data for the case retained in this study. The 17 curves correspond to the 17 thermocouple locations at which the experimental temperature measurements were compared with the simulated values (h_{bottom} = 15 W/m²/K, h_{walls} = 20 W/m²/K, and h_{top} = 7.5 W/m²/K)
Abbreviations: Ex: Experiment; Sim: Simulation

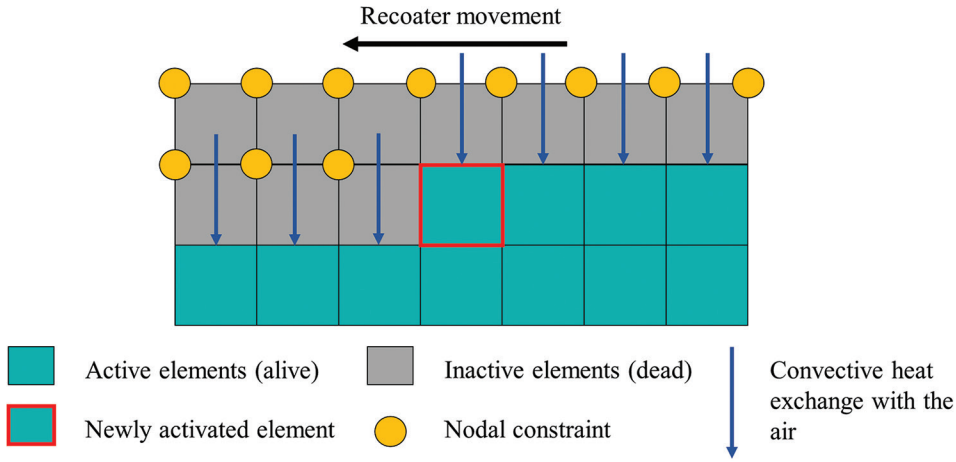

Figure 13. Schematic of the element birth and death technique coupled with the usage of nodal constraints for binder jetting during gradual powder deposition

literature,[29] such as the specific heat capacity (4.2 J/kg/K at 25°C) and thermal conductivity (0.61 W/m/K at 25°C), were used. This hypothesis was justified by the fact that the water content in the binder was above 85%. The mixture density, specific heat capacity, and thermal conductivity were obtained using the mixture law between the powder and the binder. The powder bed density was approximated to be 60%, which was considered a density approximation for 316L, based on its mass, size, and volume, whereas the remaining 40% was attributed to the binder. Considering the powder form and inclusive porosities, the mixture law takes the form as presented in Equation (7):

$$E_m = fE_W + E_p \quad (7)$$

where E_m, E_w, and E_p are the mixture, the water, and the powder properties, respectively, and f is the fraction of binder in the mixture (40%). The thermal diffusivity for the green state was obtained using the LFA 467 HyperFlash (Netzsch, Germany), whereas the specific heat capacity was measured using the Q2000 differential scanning calorimeter (TA Instruments, US). The green part's density was measured to be 4520 kg/m³, which was used to calculate thermal conductivity as per Equation (8), using thermal diffusivity α:

$$\alpha = \frac{k}{\rho c_p} \tag{8}$$

2.9. Application of the binder

The properties of the elements where the binder was applied were changed to imitate the binder deposition on loose metal powder by the printhead, as shown in Figure 3B. Equation (9) uses the heat energy transferred between the powder and the binder to compute the temperature of the mixture T_m at deposition:

$$m_w \times C_{pw} \times \left(T_m - T_w\right) = -(m_p \times C_{pp} \times \left(T_m - T_p\right)) \tag{9}$$

where T_p, T_w, and T_m are the temperatures (K) of the powder, binder, and mixture, respectively. T_p is obtained from the simulation at the time of deposition, whereas T_w was assumed to be constant and slightly higher than room temperature (27.5°C) due to marginal heating caused by the air of the chamber. C_{pp} and C_{pw} are the specific heat capacities (J/kg/K) of the powder and binder, respectively, while m_p and m_w are the masses (kg) of the powder and binder, respectively. By isolating the temperature of the mixture, Equation (9) can be rewritten as follows:

$$T_m = \frac{T_p + T_w \times \frac{m_w \times C_{pw}}{m_p \times C_{pp}}}{\left(1 + \frac{m_w \times C_{pw}}{m_p \times C_{pp}}\right)} \tag{10}$$

Using Equation (7), the masses can be obtained from the density since ratios are used in Equation (10):

$$m_w = f \times \rho_w \tag{11}$$

$$m_p = \rho_p \tag{12}$$

where ρ_p and ρ_w are the densities (kg/m^3) of the powder and binder, respectively. The deposition temperature was computed and applied to all the relevant nodes for a brief period to simulate the temperature change caused by the interaction between the powder and binder. The in-process drying driven by the lamps' heat, as shown in Figure 3A, was also represented by a change in material properties, progressing from a binder–powder mixture to the green state.

3. Results

3.1. Computational time

The computations were performed on a dual-CPU system equipped with Xeon Gold 6240 processors, operating at 2.6 GHz, using eight cores. Figure 14 shows the computational times for different numbers of layers simulated using the three models. The number of layers was 5–20 for Model 1, 20–200 for Model 2, and 200–2000 for Model 3. At this scale of comparison, the computational time increased significantly with the number of layers for all three models. Model 1 demonstrated the most rapid increase in simulation time relative to the number of elements involved, followed by a slightly lower increasing rate for Model 2 and a significantly reduced rate for Model 3. Model 1 required 28 h to simulate 20 layers. Model 2 simulated 200 layers in 33 h, whereas Model 3 showed a 10-fold increase in efficiency, simulating 2000 layers in 33 h, primarily attributable to its capability to lump 10 layers at a time compared to only one layer for Model 2.

3.2. Model validation

The surface temperatures of the powder bed were measured during the printing of 27 coupons using a thermoIMAGER TIM VGA thermal imaging camera (Micro-Epsilon, Germany) positioned above the powder bed, with a resolution of 640 × 480 pixels and a measurement error of ± 2°C. The emissivity of the infrared camera was calibrated using a thermocouple in contact with the powder bed to ensure that both the camera and the thermocouple recorded the same temperature. No significant variation of emissivity was detected between wetted and unwetted powder areas.

A representative image of the temperature distribution on the top surface of the powder bed after the binder set time of the 20th layer is shown in Figure 15A. A maximum temperature of 59°C was observed in the loose metal powder, whereas the minimum was approximately 44°C, observed in the areas of the binder–powder mixture (specimens 1 and 2). Models 1 and 2 produced results similar to those obtained from the thermal camera. Model 3 showed a similar trend, but with a slight variation in temperature ranging between 46°C and 56°C.

To better illustrate the temperature variation during BJ, three areas were selected (shown in Figure 15), and their temperatures were plotted as a function of the number of layers (Figure 16). Area 1 was positioned on loose metal powder, Area 2 on a printed specimen of Format 1, and Area 3 on a printed specimen of Format 2. In this way, two types of specimens with different build heights, 18 mm (Format 1) and 15 mm (Format 2), were examined.

From Figure 16, a slight drop in temperature was observed in Area 1 (loose powder only) during the deposition of the first 15 layers, attributed to the cooling effect of successive powder layer depositions at room temperature. This effect was more pronounced in

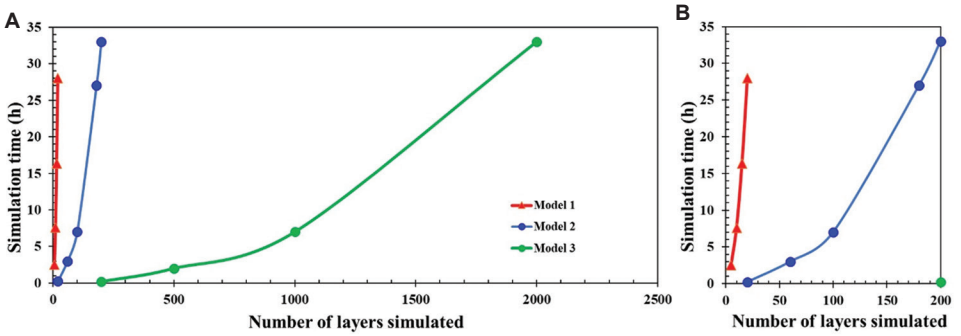

Figure 14. Computational time comparison using eight CPUs. (A) Comparison among the Models 1, 2, and 3. (B) An enlarged view of the results of Models 1 and 2

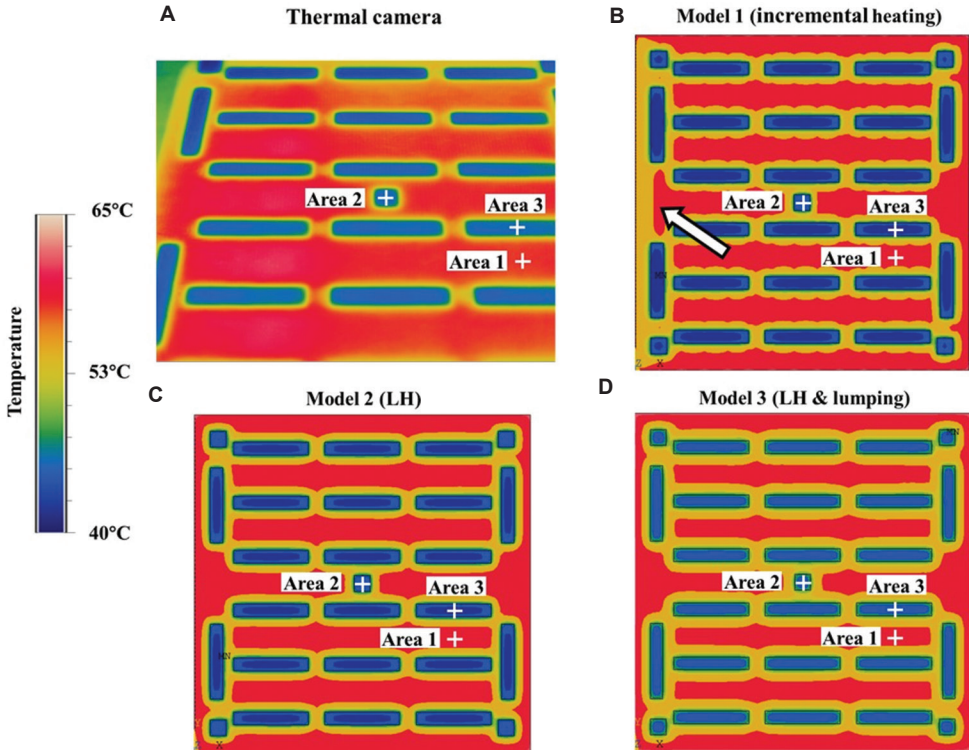

Figure 15. Comparison of the temperature distribution of the powder bed after the binder set time of the 20th layer among (A) the thermal camera measurement and the simulation results for (B) Model 1, (C) Model 2, and (D) Model 3. The three areas of interest are indicated using white plus signs, whereas the white arrow indicates a cooler zone on the left edge of the powder bed

Areas 2 and 3 (binder–powder mixture) due to increased cooling upon the deposition of the binder, driven by the higher specific heat capacity of the binder–powder mixture compared to the loose powder. After 20 layers, the temperature remained relatively stable with a slight increase observed in Area 1, primarily due to the gradual heating of metal powder within the powder bed as its volume increased, eventually equilibrating with the build box temperature. This process resulted in heat transfer through conduction between the powder beneath the surface layer and the surface itself, where the experimental data were collected. Meanwhile, Area 3 demonstrated a similar trend to Area 2 up to the 150th layer (Figure 16B) due to their comparable material properties (binder–powder mixture). After the 150th layer, the material properties of Area 3 changed from binder–powder mixture to powder only due to the printing completion of the Format 2 specimen. This led to a sharp increase in Area 3's temperature by approximately 10°C. Since the specimen 1 in Area 2 was completed only after the 180th layer, the material properties remained constant, and the temperature remained relatively stable.

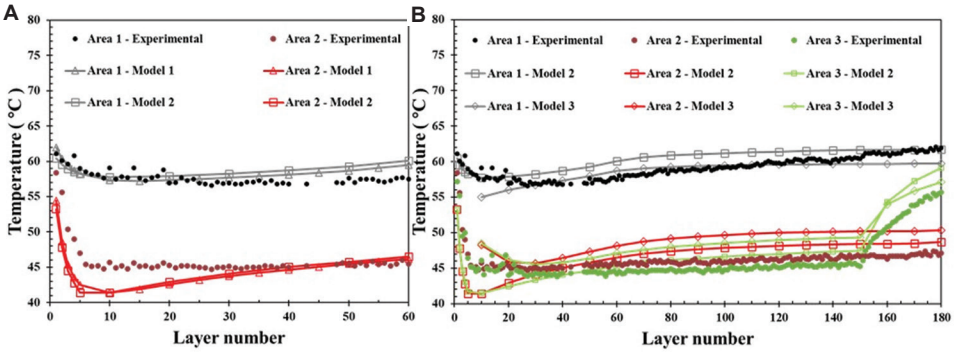

Figure 16. The temperature variation in the studied regions over (A) the initial 60 layers, as determined by experimental data and modeling results from Models 1 and 2, and (B) the first 180 layers, as determined by experimental data and modeling results from Models 2 and 3

Figure 16A presents the comparison between the temperature evolution of Areas 1 and 2 with Models 1 and 2 for the first 60 build layers. Data from Area 3 were omitted, as they did not show a distinctive behavior compared to Area 2 during the first 60 layers. The two models accurately predicted the temperature evolution in Area 1, with maximum absolute errors of 1.6°C and 2.5°C for Models 1 and 2, respectively. The two models showed a larger error when simulating Area 2. They initially fell below the experimental results by approximately 4.5°C at the 10th layer, then gradually increased, converging with the experimental data around the 30th layer. The larger variation observed within the first 10 layers can be attributed to an overestimation of the powder bed packing density, as the powder bed density was likely to vary during the deposition of the first layer. Consequently, a mis-evaluation of the binder saturation rate assumed for the process led to an inaccurate prediction of the drying conditions of the binder. Determining the precise moment at which certain properties emerge in the binder–powder mixture is inherently challenging. This difficulty arises from the dynamic process conditions varying spatially across the powder bed. The general variation observed in the model's behavior can also be attributed to the calibration of the boundary conditions coefficients, which are known to introduce errors in the temperatures predicted inside the powder bed, as discussed in Section 2.5.

Figure 16B presents the comparison between the temperature profiles of the experimental observations and the models for the first 180 layers. Model 1 was not included due to its insufficient computational efficiency. Models 2 and 3 closely matched the trends in the experimental data for Area 1, with a maximum discrepancy of just over 2.2°C for Model 2 and under 4°C for Model 3. The maximum temperature variation observed in Model 3 coincided with the first computed layer of Model 3 due to the lumping strategy employed. For Areas 2 and 3, Model 2 underestimated the temperature during the first 30 layers by up to 3°C, which is also observed in Figure 16A. This temperature difference decreased with the number of layers and turned into an overestimation of up to 2°C. Model 3, on the other hand, overestimated the first 10 layers by up to 4°C due to the 10-layer lumping strategy, then converged rapidly with Model 2 as the number of layers increased, exhibiting similar temperature profiles. The two models accurately captured the sharp temperature increase observed after the 150th layer due to the changes in material properties in Area 3.

4. Discussion

4.1. Thermal profile and computational efficiency

Model 1, with gradual powder deposition and incrementally moving heat sources, is closest in replicating the actual BJ process. As evident in Figure 15, Model 1 captured a slightly cooler area on the left side of the print bed (marked by white arrows in Figure 15B), which cannot be observed with other models. However, due to the movement of heat sources, the time discretization used became noticeable, as the cooled area around the printed specimens displayed an undulating profile. The number of layers that can be simulated using this model is severely limited due to its high computational cost, driven by the use of 40 time steps. This limitation was resolved by Model 2, which utilizes the LH method in a single time step, yielding an average absolute error of 0.6°C (Figure 17A) and reducing the calculation time for simulating 60 layers by a factor of 60 compared to Model 1. Nevertheless, this approach enables a detailed comparison with experimental data to ensure validation, but it is not sufficiently fast for a full-build simulation. Model 3 further improved the computational time, simulating 200 layers in 1/165 of the time required by Model 2 and the entire BJ process (2000 layers) in 32 h,

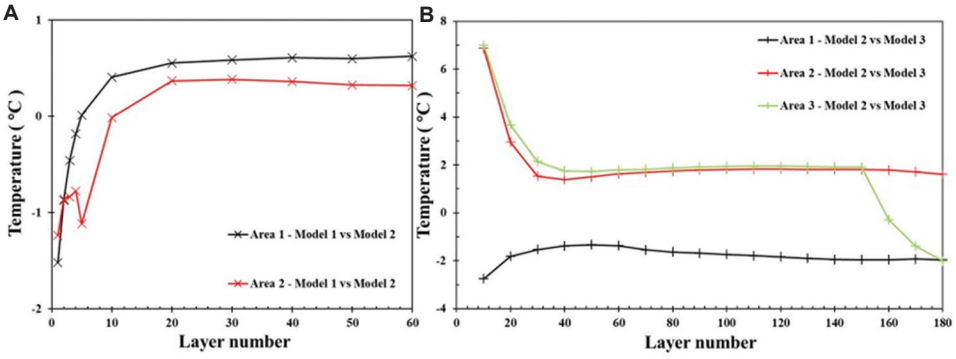

Figure 17. The temperature errors in the studied regions over (A) the initial 60 layers between the modeling results from Models 1 and 2, and (B) the first 180 layers between the modeling results from Models 2 and 3

which is slightly less than twice the process time (18 h to print the 2000 layers). These results are consistent with earlier findings reported in the literature on LPBF, where the computational time achieved using four lumped layers is three times shorter compared to the standard LH method.[23]

Figure 17B illustrates the error in temperature results from Models 2 and 3 over the 180 printed layers. The error between the models was more pronounced in the early stages of the process, which stabilized around 2°C for all areas. Transition phases where material properties or boundary conditions change are challenging to capture. For Areas 2 and 3, the first results observed for Model 3 corresponded to the 10th layer and showed an error of +7°C relative to Model 2. The first 10 layers of the experimental case were combined into a single layer, where only the conditions of the top layer in the group were used for calculations. This limited the model's ability to capture any changes in behavior occurring within the lumped group. In addition, the material change occurring at the 150th layer of printing in Area 3 constrained the number of layers that can be lumped together. The number of lumped layers must ensure that the material change coincides with the boundary between two layers of elements, thereby aligning the shift in properties within the model with the process timing.

An effective solution to these challenges involves modulating the number of lumped layers based on the simulated conditions, following a method similar to that proposed by Tangestani *et al.*[20]—developing a multiscale model for LPBF applications. Using this approach, the change in boundary conditions and materials can be accurately modeled by reducing the number of lumped layers in situations where a transient state is observed. In contrast, the calculations for the rest of the process, where a steady state is observed, can be reduced by increasing the number of lumped layers.

4.2. Challenges associated with finite element modeling

Incorporating the gradual deposition of material into FEM throughout the process is a challenging task. While using the element birth and death technique is a useful tool in FEM for simulating the AM process, certain considerations need to be taken into account when using this approach with APDL. Deactivated elements still experience temperature changes through conduction from neighboring active elements, causing the initial conditions of deactivated nodes to be lost. This requires applying nodal constraints to maintain the intended temperature. However, controlling the activation temperature is difficult because adjacent layers share common nodes that cannot be constrained. As a result, only the top nodes of newly activated elements are constrained. This induces a nodal thermal gradient across the elements, influencing the matrix calculations during the simulation, subsequently impacting the accuracy of temperature predictions at the upper surface of the powder bed. One potential solution is to introduce a thin layer of elements to act as a buffer between the activated and constrained inactive elements. This approach has the advantage of significantly reducing the nodal thermal gradient. However, it doubles the number of elements, thereby increasing the computational cost. Furthermore, a dynamic remeshing algorithm cannot be applied in this case because Ansys is unable to merge elements during the solution process.

4.3. Finite element modeling-based optimization of specimen nesting in BJ

Similarly to electron beam melting, where thermal management within the chamber is critical, a combination of numerical simulations and experimental methods facilitates a deeper understanding of the thermal processes involved in BJ.[30] During BJ printing, closely nested parts can reduce the efficiency of the drying process, as the

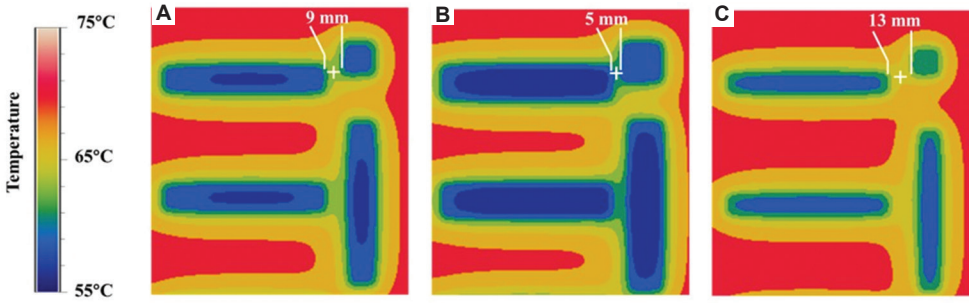

Figure 18. Impact of nesting on the temperature between the printed specimens before the application of binder on the 150th layers of printing for (A) the reference case with a 9 mm gap between specimens, (B) a smaller gap of 5 mm between specimens, and (C) a bigger gap of 13 mm between specimens. The area of interest for the comparison is indicated using a white plus sign

binder concentration increases significantly in localized regions, potentially leading to bleeding defects.[31] This work effectively utilized FEM to optimize the nesting process by establishing the effect of the inter-specimen distance on the temperature distribution in the surroundings.

The finite element model incorporated the specimen configuration and printing settings described in Figure 2, whereas the specimen sizes were varied to adjust the inter-specimen distance. Figure 18 shows the thermal distribution simulated using Model 3 in the region surrounding the smallest gap between printed specimens before the application of binder on the 150th layer. In Figure 18A, the results corresponding to the specimen dimensions used for model validation in the previous section are provided. Lower temperatures were observed in the loose powder between the specimens compared with the loose powder elsewhere in the powder bed. In Figure 18B, the gap between the specimens was reduced to 5 mm, producing a cooler and wider channel in the loose powder compared to the reference case. In Figure 18C, the gap was increased to 13 mm. Under this configuration, the temperature between the specimens of Formats 1 and 2 was higher than in their vicinity, suggesting a better thermal isolation between the specimens.

The effect of inter-specimen distance on the temperature between them is shown in Figure 19. As the center became farther from the cooled specimen, the energy loss through conduction was reduced. This resulted in a nearly linear temperature increase of 5°C as the distance increased from 5 mm to 15 mm after 150 layers. The observed temperature stability can be attributed to the heat transferred to the powder bed from heating lamps and the heated build box during printing. At approximately 65°C, the solvent in the binder partially vaporized upon deposition, causing an increase in viscosity. Under these conditions, the temperature variation observed has a negligible effect on the amount of solvent evaporated. As a result, the binder should maintain consistent properties across the entire

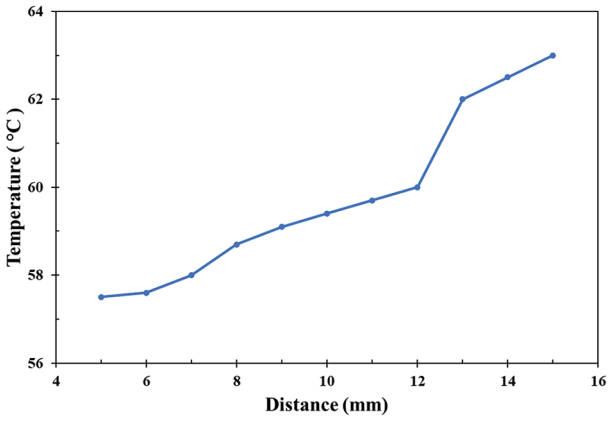

Figure 19. Temperature at the center of inter-specimen spacing before binder application on the 150th layer as a function of varying distances between printed specimens

powder bed, regardless of the nesting configuration of the printed specimen, thereby minimizing the risk of defects. A heated powder bed and lamps arranged in an H2 configuration significantly contribute to efficiently controlling thermal variations caused by binder deposition during printing. This, in turn, reduces the effect of part nesting on solvent evaporation and subsequently binder viscosity, resulting in a more evenly distributed thermal profile.

5. Conclusion

In this study, the thermal analysis of the print bed during the BJ process was performed by developing three novel finite element models employing 2D Gaussian moving heat input, LH, and lumped heating combined with LH, respectively. Results ranging from accurate heat distribution, characterized by the movement of the lamps, to the behavior of the print bed over a full print were obtained for the three models and validated using thermal data obtained from BJ printing with the same parameters. Major conclusions from this study are:

(i) The incremental heating model simulated 20 layers in 28 h. The single LH model extended this capability to 200 layers in 33 h, whereas the multiple LH model, grouping 10 layers at a time, enabled simulation of 2000 layers for the same computation time. The multiple LH model proved to be the most computationally efficient, allowing the simulation of a full BJ process.

(ii) The incremental heating model showed the highest accuracy, with an average absolute error of approximately 1.5°C compared to experimental results during the first 60 layers. The single LH model exhibited a 1.7°C error, and the multiple LH model reached 2.3°C for the 180-layer case.

(iii) The incremental heating model effectively captured local temperature variation associated with the movement of the heat sources in the printer and phase transitions during binder–powder mixing and evolving boundary conditions. The LH model offers an efficient alternative for simulating a large number of layers and similarly captures phase transitions. However, the multiple LH method, while significantly faster, sacrifices accuracy during transient states, indicating the need for a multiscale modeling approach to optimize efficiency.

(iv) Using the element birth and death technique in FEM effectively models powder layer deposition. For BJ, lower temperatures compared to fusion-based processes require precise control of nodal temperatures for newly activated elements, with nodal constraints in APDL being the most efficient solution.

(v) The proposed powder bed design—with heating elements around the build box and two infrared lamps on each side of the recoater—provides efficient thermal control. This design reduces the effects of part nesting on binder viscosity, enhancing printing repeatability by mitigating defects from binder drying variability.

Acknowledgments

None.

Funding

This study was funded by the Natural Sciences and Engineering Research Council of Canada (NSERC) under grant no. ALLRP 575177-22.

Conflicts of interest

Etienne Martin serves as the Editorial Board Member of the journal, but was not in any way involved in the editorial and peer-review process conducted for this paper, directly or indirectly. Other authors declare they have no competing interests.

Author contributions

Conceptualization: Etienne Martin, Srinivas Pendurti, Arunkumar Natarajan

Formal analysis: Leon Desgagnes, Reza Tangestani

Investigation: Leon Desgagnes, Reza Tangestani, Hongyan Miao

Methodology: Leon Desgagnes, Reza Tangestani, Etienne Martin

Software: Leon Desgagnes, Honyan Miao

Writing–original draft: Leon Desgagnes

Writing–review & editing: Waris Nawaz Khan, Etienne Martin

Ethics approval and consent to participate

Not applicable.

Consent for publication

Not applicable.

Availability of data

Data are available from the corresponding author upon reasonable request.

References

1. Manjhi SK, Sekar P, Bontha S, Balan ASS. Additive manufacturing of magnesium alloys: Characterization and post-processing. *Int J Lightweight Mater Manuf*. 2024;7(1):184-213.

doi: 10.1016/j.ijlmm.2023.06.004

2. Mostafaei A, Ghiaasiaan R, Ho IT, *et al*. Additive manufacturing of nickel-based superalloys: A state-of-the-art review on process-structure-defect-property relationship. *Prog Mater Sci*. 2023;136:101108.

doi: 10.1016/j.pmatsci.2023.101108

3. Zhu Z, Hu Z, Seet HL, *et al*. Recent progress on the additive manufacturing of aluminum alloys and aluminum matrix composites: Microstructure, properties, and applications. *Int J Mach Tools Manuf*. 2023;190:104047.

doi: 10.1016/j.ijmachtools.2023.104047

4. Karimialavijeh H, Ghasri-Khouzani M, Das A, Pröebstle M, Martin É. Effect of laser contour scan parameters on fatigue performance of A20X fabricated by laser powder bed fusion. *Int J Fatigue*. 2023;175:107775.

doi: 10.1016/j.ijfatigue.2023.107775

5. Im S, Ghasri-Khouzani M, Muhammad W, *et al*. Evaluation of different sintering agents for binder jetting of aluminum alloy. *J Mater Eng Perform*. 2023;32(21):9550-9560.

doi: 10.1007/s11665-023-07829-1

6. Mirzababaei S, Pasebani S. A review on binder jet additive

manufacturing of 316L stainless steel. *J Manuf Mater Process*. 2019;3(3):82.

doi: 10.3390/jmmp3030082

7. Li M, Du W, Elwany A, Pei Z, Ma C. Metal binder jetting additive manufacturing: A literature review. *J Manuf Sci Eng*. 2020;142:090801.

doi: 10.1115/1.4047430

8. Zhao K, Su Z, Ye Z, *et al*. Review of the types, formation mechanisms, effects, and elimination methods of binder jetting 3D-printing defects. *J Mater Res Technol*. 2023;27:5449-5469.

doi: 10.1016/j.jmrt.2023.11.045

9. Onler R, Koca AS, Kirim B, Soylemez E. Multi-objective optimization of binder jet additive manufacturing of Co-Cr-Mo using machine learning. *Int J Adv Manuf Technol*. 2022;119(1):1091-1108.

doi: 10.1007/s00170-021-08183-z

10. Boillat E, Kolossov S, Glardon R, Loher M, Saladin D, Levy G. Finite element and neural network models for process optimization in selective laser sintering. *Proc Inst Mech Eng Part B J Eng Manuf*. 2004;218(6):607-614.

doi: 10.1243/0954405041167121

11. Krol TA, Seidel C, Schilp J, Hofmann M, Gan W, Zaeh MF. Verification of structural simulation results of metal-based additive manufacturing by means of neutron diffraction. *Phys Procedia*. 2013;41:849-857.

doi: 10.1016/j.phpro.2013.03.158

12. Zhang K, Zhang W, Brune R, *et al*. Numerical simulation and experimental measurement of pressureless sintering of stainless steel part printed by binder jetting additive manufacturing. *Addit Manuf*. 2021;47:102330.

doi: 10.1016/j.addma.2021.102330

13. Lee Y, Nandwana P, Simunovic S. Powder spreading, densification, and part deformation in binder jetting additive manufacturing. *Prog Addit Manuf*. 2022;7(1):111-125.

doi: 10.1007/s40964-021-00214-1

14. Chen Z, Li F, Chen W, Zhu D, Fu Z. Numerical simulation of particle size influence on the sintering behavior of 316L stainless steel powders fabricated by binder jet 3D printing. *J Mater Eng Perform*. 2021;30(5):3705-3717.

doi: 10.1007/s11665-021-05709-0

15. Luo Z, Zhao Y. A survey of finite element analysis of temperature and thermal stress fields in powder bed fusion additive manufacturing. *Addit Manuf*. 2018;21:318-332.

doi: 10.1016/j.addma.2018.03.022

16. Schoinochoritis B, Chantzis D, Salonitis K. Simulation of metallic powder bed additive manufacturing processes with the finite element method: A critical review. *Proc Inst Mech Eng Part B J Eng Manuf*. 2017;231(1):96-117.

doi: 10.1177/0954405414567522

17. Zhang Z, Huang Y, Rani Kasinathan A, *et al*. 3-Dimensional heat transfer modeling for laser powder-bed fusion additive manufacturing with volumetric heat sources based on varied thermal conductivity and absorptivity. *Opt Laser Technol*. 2019;109:297-312.

doi: 10.1016/j.optlastec.2018.08.012

18. Goldak J, Chakravarti A, Bibby M. A new finite element model for welding heat sources. *Metall Trans B*. 1984;15(2):299-305.

doi: 10.1007/BF02667333

19. Roberts IA, Wang CJ, Esterlein R, Stanford M, Mynors DJ. A three-dimensional finite element analysis of the temperature field during laser melting of metal powders in additive layer manufacturing. *Int J Mach Tools Manuf*. 2009;49(12):916-923.

doi: 10.1016/j.ijmachtools.2009.07.004

20. Tangestani R, Chakraborty A, Sabiston T, Yuan L, Ghasri-Khouzani M, Martin É. Multi-scale model to simulate stress directionality in laser powder bed fusion: Application to thin-wall part failure. *Mater Des*. 2023;232:112147.

doi: 10.1016/j.matdes.2023.112147

21. Thorborg J, Esser P, Bayat M. Thermomechanical modeling of additively manufactured structural parts - different approaches on the macroscale. *IOP Conf Ser Mater Sci Eng*. 2020;861(1):012008.

doi: 10.1088/1757-899X/861/1/012008

22. Bayat M, Klingaa CG, Mohanty S, *et al*. Part-scale thermo-mechanical modelling of distortions in laser powder bed fusion - analysis of the sequential flash heating method with experimental validation. *Addit Manuf*. 2020;36:101508.

doi: 10.1016/j.addma.2020.101508

23. An K, Yuan L, Dial L, Spinelli I, Stoica AD, Gao Y. Neutron residual stress measurement and numerical modeling in a curved thin-walled structure by laser powder bed fusion additive manufacturing. *Mater Des*. 2017;135:122-132.

doi: 10.1016/j.matdes.2017.09.018

24. Lee H, Lim CHJ, Low MJ, Tham N, Murukeshan VM, Kim YJ. Lasers in additive manufacturing: A review. *Int J Precis Eng Manuf-Green Technol*. 2017;4(3):307-322.

doi: 10.1007/s40684-017-0037-7

25. Mills KC. *Recommended Values of Thermophysical Properties for Selected Commercial Alloys*. United Kingdom: Woodhead Publishing; 2002.

26. Imani Shahabad S, Karimi G, Toyserkani E. An extended rosenthal's model for laser powder-bed fusion additive manufacturing: Energy auditing of thermal boundary conditions. *Lasers Manuf Mater Process*. 2021;8(3):288-311.

doi: 10.1007/s40516-021-00148-0

27. ANSYS. *Advanced Analysis Guide*. United States: ANSYS; 2022.
28. Van Nguyen C. *Numerical Simulation of Hot Isostatic Pressing with Particular Consideration of Powder Density Distribution and Temperature Gradient*. Vol 11. Germany: Shaker Verlag; 2016.
29. Peng W, Jizu L, Minli B, Yuyan W, Chengzhi H. A Numerical Investigation of Impinging Jet Cooling with Nanofluids. *Nanoscale Microscale Thermophys Eng*. 2014;18:329-353.

doi: 10.1080/15567265.2014.921749

30. Landau E, Tiferet E, Ganor YI, *et al*. Thermal characterization of the build chamber in electron beam melting. *Addit Manuf*. 2020;36:101535.

doi: 10.1016/j.addma.2020.101535

31. Crane NB. Impact of part thickness and drying conditions on saturation limits in binder jet additive manufacturing. *Addit Manuf*. 2020;33:101127.

doi: 10.1016/j.addma.2020.101127